# Assessment of advanced Taylor models, the Taylor factor and yield-surface exponent for FCC metals

K. Zhang[1,2], B. Holmedal[1], T. Mánik[1], A. Saai[3]

[1.] Department of Materials Science and Engineering, Norwegian University of Science and Technology, NO-7491 Trondheim, Norway

[2.] Innovation & Technology – Europe, Extruded Solutions, Hydro, SE-61281 Finspång, Sweden.

[3.] SINTEF Industry, Department of Materials and Nanotechnology, NO-7465 Trondheim, Norway

## Abstract

High-resolution crystal plasticity-finite element method (CPFEM) simulations are performed to provide new reference values of the Taylor factor $M$ and the isotropic yield surface exponent $a$ for high stacking fault energy face-centred-cubic (FCC) polycrystalline metals with random orientations. The visco-plastic Taylor factor with strain rate sensitivity $\tilde{M}$ is introduced and linearly extrapolated to its zero strain rate sensitivity limit to give the new reference value of $M$. The linear extrapolation technique is also employed to define the new reference value of $a$. The obtained new reference values are 2.7 and 6.9, for $M$ and $a$, respectively, which are much smaller than the reference values currently used for FCC materials based on full constraint (FC) Taylor model calculations, i.e. 3.07 for $M$ and 8 for $a$. Other state-of-the-art Taylor-type models, e.g. ALamel, ALamel with the type III relaxation (ALamel-T3) and the visco-plastic self-consistent (VPSC) models, can also give values for $M$ and $a$ much smaller than the FC-Taylor calculations. The performance of the CPFEM and these state-of-art Taylor-type models in terms of resolving deformation and stress fields within the aggregate can only be assessed in a statistical manner since all are statistical aggregate models. Selected statistical distributions are analysed for all models, by means of local deviations of the velocity gradient tensor, of the plastic deformation-rate tensor and of the stress tensor etc., for uniaxial tensile deformation. The ALamel models are found to provide similar statistics as CPFEM, whereas the VPSC model results are

qualitatively different. The intra-grain analysis for CPFEM demonstrates that the intra-grain interactions are as much important as the local interactions at the grain boundaries.

**Keywords**: CP-FEM; Advanced Taylor-type models; Taylor factor; Yield function exponent; Statistical analysis

## 1 Introduction

The basic simplifying assumption of the full constraint (FC) Taylor model (Taylor, 1938) is that each single grain in an aggregate crystalline is subject to the same deformation as the entire grain aggregate. The FC-Taylor model cannot account for the shape of grains and their mutual interactions. However, the grain interactions are important for reliable predictions of the texture evolution. To incorporate the effect of grain interactions, and release the full constraints imposed by the FC-Taylor theory, advanced Lamel-type models (Mánik and Holmedal, 2013; Van Houtte et al., 2005) and visco-plastic self-consistent model (VPSC) (Lebensohn and Tomé, 1993, 1994; Molinari et al., 1987) were proposed. The ALamel-type models consider the local interactions at grain boundaries, while the VPSC model considers the long-range grain and matrix interactions. Neither of these models are full-field models (Zhang et al., 2015); but they demonstrated better performance compared to the FC-Taylor model in terms of texture evolution and plastic anisotropy predictions (Mánik and Holmedal, 2013; Zhang et al., 2015). Another approach to account for the grain interactions uses the crystal plasticity model with the finite element method (CPFEM) as pioneered by Peirce et al. (1982), for a recent overview, see Roters et al. (2010). The CPFEM approach is a full-field model which resolves the grain shapes in details and accounts properly for grain interactions when a sufficiently fine mesh resolution is applied. Both strain compatibility and stress equilibrium are fulfilled at grain boundaries, at least in a weak form (Roters et al., 2010). The importance of grain interactions in a detailed CPFEM calculations is reported by Kanjarla et al. (2010). It is mentioned that more advanced n-site VPSC models have been formulated to account for local grain interactions, as first suggested by Canova et al. (1992). This type of model is a compromise between the computer-effective Taylor models and the detailed CPFEM. These models come in many versions involving a variety of complex approximations,

e.g. dependency on the mesh and the number of neighbour grains accounted for. Hence, their accuracy as compared to CPFEM can vary between the 1-site VPSC model and a full CPFEM.

The Taylor factor *M* and the yield surface exponent $a$ for polycrystalline materials are the most important parameters connecting continuum plasticity theories to crystal plasticity (CP) theories. The Taylor factor $M$ relates the equivalent flow stress $\sigma$ to the critical resolved shear stress $\tau^c$ of slip systems: $\sigma = M\tau^c$ (Bishop and Hill, 1951b). As explained in Kocks (1958) it is used in microstructurally based models to estimate strength contribution from dislocations, e.g. Hughes and Hansen (2018), from elements in solid solution, e.g. Vilamosa et al. (2016) and from precipitates, e.g. Holmedal (2015). The equivalent stress in a continuum plasticity formulation is calculated from the yield surface, and is equivalent to the stress of a tensile test in a reference direction. As introduced by Taylor (1956), the Taylor factor is defined for a uniaxial tensile test and for a rate-independent $\tau^c$ that is equal for all slip systems. To overcome the Taylor ambiguity, rate-dependent visco-plastic solutions of the slip activity (Peirce et al., 1983) have been widely employed. Even though the strain rate sensitivity at room temperature is weak, the rate-dependent models are commonly used because they provide stable and unambiguous numerical implementations.

According to the Taylor model, the equivalent strain rate $\dot{\varepsilon}$ is related to the algebraic sum of the resolved shear strains rate by $\dot{\varepsilon} = \dot{\gamma} / M$, where $\dot{\gamma} = \sum_{\alpha} \left| \dot{\gamma}^{\alpha} \right|$. As a result, the strain hardening slope $d\sigma/d\varepsilon$ is proportional to $M^2$, and therefore sensitive to the assumed value of $M$ (Mecking et al., 1996). The Taylor factor cannot be directly measured from experiments, but it can be calculated or estimated using crystal plasticity models. For high stacking-fault energy face-centred cubic (FCC) polycrystalline metals with random orientations, the reference value $M = 3.07$ was obtained for uniaxial tensile deformation by the full constraint (FC) Taylor model, also referred to as the Taylor-Bishop-Hill model (Bunge, 1970; Kocks, 1970; Taylor, 1938; Taylor and Dehlinger, 1956). This value has been accepted as a reference value in the literature for analysing or establishing strain-hardening laws for FCC metals with a random, weak texture, or even for an unspecified texture e.g. Blum and Zeng (2009), Kocks and Mecking (2003) and Zhao and Holmedal (2013). Most models include parameters that

can be re-tuned to match a lower value of the Taylor factor. However, recent multiscale models are "parameter free", e.g. the model for solute strengthening by Leyson et al. (2010), or the model for precipitate strengthening by Holmedal (2015).

In classical plasticity theory, plastic deformation is assumed to take place when the stress tensor satisfies a certain condition defined by the yield criterion or yield function. Various yield functions were developed for polycrystalline materials in which, the exponent $a$ is regarded as a material coefficient related to the crystal structure. As an example, a high-exponent isotropic yield function was proposed by Hershey (1954) and later used by Hosford (1972) for cubic crystal metals:

$$f(\boldsymbol{\sigma}) = 2^{-\frac{1}{a}}\left(\left|\sigma_1-\sigma_2\right|^a+\left|\sigma_2-\sigma_3\right|^a+\left|\sigma_3-\sigma_1\right|^a\right)^{\frac{1}{a}}-\sigma_Y, \qquad (1)$$

where $\boldsymbol{\sigma}$ is the Cauchy stress tensor, $\sigma_1$, $\sigma_2$ and $\sigma_3$ are the corresponding major stresses and $\sigma_Y$ is the yield stress. Based on Taylor-Bishop-Hill calculations, Barlat (1987) estimated the exponent $a$ to be 5.81 with pencil glide for body-centred-cubic (BCC) and 8.95 for $\{111\}<110>$ slip in FCC metals. Many anisotropic yield functions have been proposed based on the formulation of the Hershey isotropic yield functions, and can be found in the review of Banabic (2010). Barlat et al. (1991) and Karafillis and Boyce (1993) proposed advanced yield functions using linear transformations of the stress tensors. These yield functions describe the complex plastic anisotropic behaviour of aluminium alloys with a surprisingly low number of calibrated parameters (Aretz and Barlat, 2013; Banabic et al., 2005; Barlat et al., 2005). The exponent $a$ in these anisotropic yield functions are commonly rounded to its closest even integer value, i.e. $a$=6 for BCC metals and $a$=8 for FCC metals. The value of the exponent $a$ influences the shape of yield surfaces both for the Hershey isotropic and its related anisotropic yield functions. The shape of yield surfaces has a major influence on the plastic behaviour and formability of metals (Barlat, 1987; Barlat and Richmond, 1987). This makes the exponent $a$ a fundamental parameter for the continuum plasticity when applying Hershey-type isotopic or linear transformation based anisotropic yield functions. Accurate references values are vital.

The value of the exponent $a$ depends on the texture when a calibration is made for a considered section of the yield surface. A strong and narrow cube texture gives a very

high exponent, whereas a 15 degree spread of the cube texture is known to give a rounded yield surface for the section with normal stress in the rolling direction versus the transverse direction (Wu et al., 2004). In the linear stress transformation based anisotropic yield surfaces this can partly be accounted for in this section, whereas the overall behaviour of the yield surface in the other portions of the stress space corresponds to the exponent for the case of random orientations as a first order estimate. Hence, relevant experiments to determine an overall recommended value of $a$ for linear transformation based yield surfaces should be on alloys with a weak texture or random orientations. An example of an earlier work, reporting a quadratic initial yield surface is by Shiratori and Ikegami (1968) for the case of alpha Brass. However, most recent works assume $a=8$ based on the Taylor model prediction. Dunand et al. (2012) found a good agreement with $a=8$ and the Yld2000 yield function for the case of extruded aluminium AA6260-T6 sheets. However, contributions to anisotropy is expected both from texture and the precipitates (Han et al., 2004). Kuwabara et al. (2005) and Kuwabara (2007) reported good agreement for an AlMg alloy (AA5154-H112) with the same yield function. However, in a recent work on another annealed, weakly textured AA5754-O alloy, the calibration of the Yld2000 yield surface with an exponent equal to 8 underestimated the plane strain portion of the yield surface. This could be caused by a too high value of exponent $a$ (Iadicola et al., 2008). For O-temper AlMg2.5 and AlMg5.5 alloys, Kuwabara et al. (2006) reported a better fit to the Hersey yield function with $a=6$ than with $a=8$, based on tensile tests results, assumingly with a weak texture. Most recent works are strongly biased or simply assumes that the exponent equals 8 as predicted by the Taylor model for FCC. It is therefore important to validate this assumption experimentally and by more advanced crystal plasticity calculations.

It was reported by Zhang et al. (2015) that the Taylor factor $M$ of uniaxial deformations and the yield surface exponent $a$ for FCC polycrystalline metals with random orientations, as predicted by ALamel-type models and by one specific homogenization variant of the VPSC model, were considerably smaller than the values predicted by the FC-Taylor model. These models are based on the same Schmid assumption (Schmid and Boas, 1935) as the CPFEM, but with severe simplifying assumptions that strongly reduce the computational costs. The Taylor factor was estimated to be $M$=2.7 from viscoplastic CPFEM simulations by Tadano et al. (2012) using a small rate sensitivity of $m$=0.002. They compared the results to FC-Taylor model predictions and found that

in CPFEM each grain had a wide distribution of strains. They concluded that the effect of the grain shape is small when the number of grains is sufficiently large, and that at least 200 grains are required to represent the behaviour of FCC polycrystalline metals. The ALamel-type models and the VPSC model provide surprisingly good results, compared to CPFEM, and to experiments. However, no systematic study has been performed on how much their solutions differ from CPFEM calculations.

Rate-independent CPFEM implementations exist, e.g. Yoshida and Kuroda (2012). As discussed by Mánik and Holmedal (2014), one of the ambiguity solutions corresponds to the limit of vanishing strain rate sensitivity of the yield surface model. One way to approximate this natural limit case is to apply a regularized yield surface for the crystal, as in Zecevic and Knezevic (2018). However, too high exponents of the regularized crystal yield surface cause numerical instabilities. A way to still approximate the rate-independent limit would be to extrapolate such solutions towards an infinite exponent. Instead, in this work, a rate-dependent CPFEM modelling framework is employed to determine Taylor factor $M$ and yield surface exponent $a$. When comparing the CPFEM solutions to the rate-independent FC-Taylor models, the CPFEM solutions are carefully extrapolated to their rate-independent limit. Furthermore, the influence of the mesh resolution is accounted for. The rate-dependent crystal plasticity framework and its numerical integration method are briefly outlined in Section 2. An adequate extrapolation procedure of the Taylor factor towards the strain rate independent limit for visco-plastic models is developed and explained in Section 3. The simulations of uniaxial tensile and different in-plane loading are performed by CPFEM with various mesh resolutions in order to estimate the reference values of Taylor factor $M$ and the isotropic yield function exponent $a$ (Section 4). The validity of the advanced Taylor models is assessed in Section 5 through analyses of their statistical predictions as compared to CPFEM. Results are further discussed in Section 6 before the conclusions in Section 7.

## 2 CPFEM modelling framework

The model formulation is limited to small elastic strains and isochoric plasticity. The corotational stress approach is applied. This section outlines the main constitutive relations describing CPFEM modelling framework which is described in more details in Zhang et al. (2014b).

The velocity gradient tensor $\mathbf{L}$ is additively decomposed into symmetric and skew-symmetric parts:

$$\mathbf{L} = \mathbf{D} + \mathbf{W}, \tag{2}$$

where $\mathbf{D}$ is the symmetric deformation rate tensor and $\mathbf{W}$ is the skew-symmetric spin rate tensor. The tensors $\mathbf{D}$ and $\mathbf{W}$ are further decomposed into lattice and plastic parts:

$$\mathbf{D} = \mathbf{D}^e + \mathbf{D}^p, \tag{3}$$

$$\mathbf{W} = \mathbf{W}^* + \mathbf{W}^p, \tag{4}$$

where $\mathbf{D}^e$ is the elastic deformation rate and $\mathbf{D}^p$ is the plastic deformation rate due to crystallographic slip. The spin tensors $\mathbf{W}^*$ and $\mathbf{W}^p$ represent the lattice and plastic spins, respectively. The plastic deformation rate and spin tensors depend on the slip rates for the active slip systems, and are respectively defined as

$$\mathbf{D}^P = \sum_\alpha \dot{\gamma}^\alpha \mathbf{P}^\alpha \quad \text{with} \quad \mathbf{P}^\alpha = \frac{1}{2}(\mathbf{m}^\alpha \otimes \mathbf{n}^\alpha + \mathbf{n}^\alpha \otimes \mathbf{m}^\alpha), \tag{5}$$

$$\mathbf{W}^P = \sum_\alpha \dot{\gamma}^\alpha \mathbf{\Omega}^\alpha \quad \text{with} \quad \mathbf{\Omega}^\alpha = \frac{1}{2}(\mathbf{m}^\alpha \otimes \mathbf{n}^\alpha - \mathbf{n}^\alpha \otimes \mathbf{m}^\alpha), \tag{6}$$

where $\dot{\gamma}^\alpha$ is the shear rate of slip system $\alpha$, $\mathbf{m}^\alpha$ is the unit vector defining slip direction and $\mathbf{n}^\alpha$ is the unit slip plane normal vector, for the slip system $\alpha$. The vectors $\mathbf{m}^\alpha$ and $\mathbf{n}^\alpha$ are not affected by crystallographic slip but will be rotated by the lattice spin $\mathbf{W}^*$ as:

$$\dot{\mathbf{m}}^\alpha = \mathbf{W}^* \cdot \mathbf{m}^\alpha, \quad \dot{\mathbf{n}}^\alpha = \mathbf{W}^* \cdot \mathbf{n}^\alpha. \tag{7}$$

A hypo-elastic relation is used here and the rate of the Cauchy stress tensor $\boldsymbol{\sigma}$ is defined as

$$\dot{\boldsymbol{\sigma}} = \boldsymbol{\sigma}^{\nabla J} + \mathbf{W}^* \cdot \boldsymbol{\sigma} - \boldsymbol{\sigma} \cdot \mathbf{W}^*, \tag{8}$$

where the Jaumann stress rate tensor $\boldsymbol{\sigma}^{\nabla J}$ is computed as

$$\boldsymbol{\sigma}^{\nabla J} = \mathfrak{R} \cdot \left[ \hat{\mathbf{C}} : \left( \mathfrak{R}^T \cdot \mathbf{D}^e \cdot \mathfrak{R} \right) \right] \cdot \mathfrak{R}^T. \tag{9}$$

In Eq. (9), $\hat{\mathbf{C}}$ is the fourth-order elasticity tensor which is constant in the co-rotational lattice frame, whereas $\mathfrak{R}$ is the rotation tensor from the initial crystal frame to the current co-rotational frame:

$$\dot{\mathfrak{R}} = \mathbf{W}^{*} \cdot \mathfrak{R} . \tag{10}$$

In the case of rate-dependent crystal-plasticity approach, all slip systems are active and the slip activity of each slip system $\dot{\gamma}^{\alpha}$ in Eqs. (5) and (6) is determined by a power-law-type equation:

$$\frac{\dot{\gamma}^{\alpha}}{\dot{\gamma}_0} = \left| \frac{\tau^{\alpha}}{\tau_0} \right|^{\frac{1}{m}} \operatorname{sgn}(\tau^{\alpha}) . \tag{11}$$

The parameter $\tau_0$ which scales the slip resistance, is given a constant value in this work. The parameter $\dot{\gamma}_0$ is a reference shearing rate which scales the shear strain rate on each slip system, $m$ is the instantaneous strain rate sensitivity and $\tau^{\alpha}$ is the resolved shear stress which is linked to the current stress-state by:

$$\tau^{\alpha} = \boldsymbol{\sigma} : \mathbf{P}^{\alpha} \tag{12}$$

It should be mentioned here that an adaptive sub-stepping integration scheme with the modified Euler method (Zhang et al., 2014b) was used. This integration scheme is extremely robust and efficient, for which the instantaneous strain rate sensitivity *m* can set to a value as low as $10^{-5}$ to explore the very nearly rate-independent stress-strain response. A rate-dependent Taylor model has also been implemented as a stand-alone code.

## 3 Taylor factor by rate-dependent models

### 3.1 Visco-plastic Taylor factor

For the rate-independent Taylor type crystal plasticity models, the Taylor factor can be defined as the ratio between the flow stress out of uniaxial tensile tests and the critical resolved shear stress $\tau_c$

$$M = \frac{\sigma}{\tau_c}. \tag{13}$$

However, this definition is not meaningful for rate-dependent models, where the resolved shear stress depends on the resolved shear strain rate. Even when the strain rate sensitivity is low, the resolved shear stresses of the active slip systems are slightly different, depending on their corresponding slip rates. In other words, the uniaxial yield stress $\sigma$ is influenced by $\dot{\gamma}_0$, $\tau_0$ and $m$ for a prescribed global deformation rate $\mathbf{D}$ (see Eq. (11)). In the limit of vanishing strain rate sensitivity, i.e. when $m \to 0$, the rate-dependent formulation degenerates smoothly into a solution of the rate-independent model, but with one particular solution of the Taylor ambiguity (Mánik and Holmedal, 2014). Note that all ambiguity solutions have the same Taylor factor. The estimation of the rate-independent limit in Eq. (13) requires $m$ to be very small, which introduces numerical stability and convergence problems making computations very challenging.

It is noted from a dimensional analysis, see Appendix A, that the parameters $\dot{\gamma}_0$, $m$ and $\tau_0$ do not enter the problem formulation independently, but can without loss of generality be grouped together. The strain rate $D_{11}$, which corresponds to the equivalent strain rate of a uniaxial tensile test, is applied as an external scale of the problem. As a result of this dimensional analysis, a visco-plastic Taylor factor for strain rate sensitivity, $\tilde{M}$, is introduced in this work and defined as:

$$\tilde{M} = \frac{\sigma_{11}}{\tau_0} \cdot \left( \frac{\dot{\gamma}_0}{D_{11}} \right)^m . \tag{14}$$

It follows from this analysis that the strain rate dependency of the visco-plastic Taylor factor $\tilde{M}$ is only related to the chosen value of $m$.

### 3.2 Extrapolation of the visco-plastic Taylor factor towards *m=0*

As $m$ is approaching its zero-limit, the visco-plastic Taylor factor with strain rate sensitivity ($\tilde{M}$) will approach the value of Taylor factor $M$ by the rate-independent calculations, i.e. $\lim_{m \to 0} \tilde{M}(m) = M$. The value of $\tilde{M}(m)$ can be determined for a specific

texture and tensile direction. Instead of trying to calculate $\tilde{M}(m)$ for extremely small values of *m*, it will be linearly extrapolated towards the limit *m=0*.

$$\tilde{M}(m) = M + A \cdot m \tag{15}$$

Here $A$ is a constant and $M$ is the Taylor factor in the limit $m \to 0$. Both $A$ and $M$ are functions of the crystallographic texture, the tensile test direction and the homogenization method. The values of parameters *M* and *A* can be calibrated according to Eq. (15) with at least two different data points calculated on the $\tilde{M}(m)$ curve.

### 3.3 Validation of the proposed extrapolation towards *M*

In order to validate the use of Eq.(15) for extrapolation of $\tilde{M}(m)$ towards $M$, a detailed investigation including very small values of $m$ was made. The rate-dependent Taylor model was applied instead of CPFEM for this section, to reduce the computational effort.

A total of 1000 grains with random orientations were simulated under uniaxial tensile deformations. Isotropic elasticity was assumed where the values of elasticity constants are referred to Zhang et al. (2014b). The values for $\tau_0$, $\dot{\gamma}_0$ and the tensile test strain rate ($\dot{\varepsilon} = D_{11}$) were arbitrarily chosen. According to the dimensional analysis (see Appendix A) any combination of $\tau_0$, $\dot{\gamma}_0$ and tensile strain rate will result in the same $\tilde{M}(m)$. The simulations were stopped at a true strain of 1%. The average of the flow stress for true strains between 0.04 and 0.07 was taken as the flow stress $\sigma$ of the material. During this strain range the texture evolution can be ignored. The calculations were made with different values of *m* ($10^{-5}$, $10^{-4}$, $10^{-3}$, $5 \cdot 10^{-3}$, $10^{-2}$ and $5 \cdot 10^{-2}$).

Figure 1 plots the data points of $\tilde{M}(m)$ for all simulated cases. The relationship $\tilde{M}(m) = 3.067 - 1.58 \cdot m$ was found to fit the data in Figure 1. It is clearly seen that $M = 3.067$ is obtained, which is the same as from classical rate-independent FC-Taylor calculations.

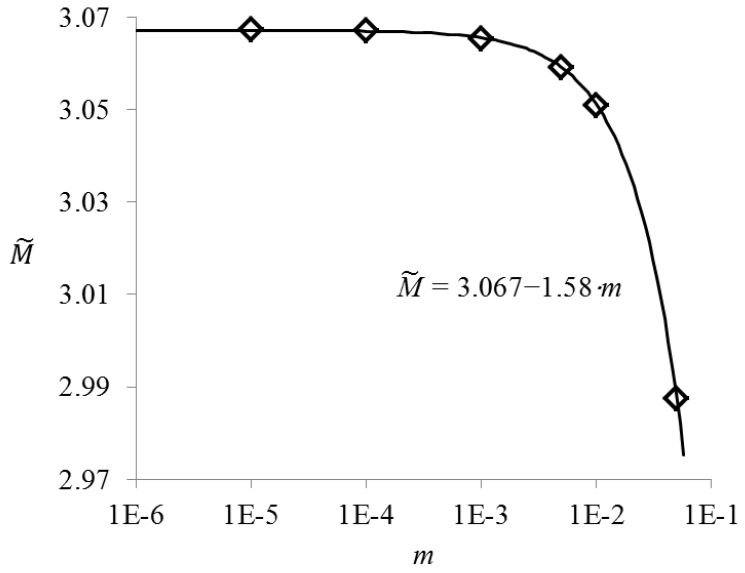


Figure 1. Data points of $\tilde{M}$ calculated by rate-dependent FC-Taylor code, for random orientations without work hardening. The solid black line represents the linear extrapolation function by Eq. (15).

Due to the existence of the visco-plastic potential, iso-values of $\dot{W} = \mathbf{D}^{\mathrm{p}} : \boldsymbol{\sigma}$ defines a shape-invariant flow surfaces that expands with increasing $\dot{W}$. In the rate insensitive limit, where $m \to 0$, all these surfaces degenerates into the rate-independent yield surface (when normalized). Hence a normalized flow surface for an arbitrary iso-value $\dot{W}$ converges towards the normalized rate-independent yield surface for sufficiently small values of $m$.

## 4 CPFEM simulations

A cube of volume $1\times1\times1\mathrm{mm}^3$ composed of 1000 grains was considered as a representative volume element (RVE) of the material in the CPFEM. The number of grains in this RVE is supposed to be sufficient to compute the effective stress states in materials having random orientations (Lequeu et al., 1987; Saai et al., 2013; Tadano et al., 2012). These same crystallographic orientations (random orientations) were used for the grain in this section and in the previous section (section 3.3). In order to investigate the influence of grain discretization on the values of *M* and *a*, the RVE was discretized in different ways, see Figure 2. First, the RVE was discretised into 1000

equi-cube elements representing the grains (Figure 2a). The grain orientations were randomly assigned to the RVE elements. One-integration-point per element and eight integration points per element were applied to this RVE. The first option (one-integration point) was applied for the sake of comparison to the Taylor models. The RVEs shown in Figure 2 (b) to (f) were then generated using the Voronoi tessellation (Quey et al., 2011) and discretized with eight-node-cubic elements and with increasing resolution from Figure 2 (b) to (f). Elements with eight integration points (Gauss points) were applied in these RVE. Periodic boundary conditions (Saai et al, 2013) were applied to all RVE in order to ensure periodicity in displacements and minimize constraint effects. It was checked that the texture, accounting for the grain size variation, remained close to that of random orientations, with a maximum intensity of about 2 times random in the orientation distribution functions corresponding to each mesh in Figure 2. Taylor factors were calculated with the FC-Taylor model for all cases and varied very little between 3.067 and 3.069.

### 4.1 Taylor factor by CPFEM simulations

Uniaxial tensile loads (Saai et al, 2013) were applied to the RVEs presented in Figure 2. In the FE simulations, the displacement speed was increased gradually from zero to 0.005 mm/s for RVEs during the first second and was then kept constant until the simulation ended at an engineering strain of 1%. Hence, the stable loading rate was $D_{11}^{\mathrm{p}} = 5 \cdot 10^{-3}\ \mathrm{s}^{-1}$. The reference shear rate $\dot{\gamma}_0$ was arbitrarily set to $10^{-3}\ \mathrm{s}^{-1}$; the critical resolved shear stress $\tau_0$ was given a value of 10 MPa, similar as in the stand-alone code simulations in Section 3.3. Three different values of the strain rate sensitivity $m$ = 0.001, 0.005 and 0.01, were used for all RVEs.

In a similar way as for the Taylor model, the flow stress for the Taylor factor calculations was determined as the average of the flow stresses between true strains of 0.04 and 0.07. The data points of $\tilde{M}\left(m\right)$ were determined and are shown in Figure 3. Eq. (15) was calibrated from these data points. The corresponding extrapolated Taylor factor $M$ is listed in Table 1. The total number of integration points indicated in Figure 3 and Table 1 is given by multiplying the number of elements in the RVE and the number of integration points per element, e.g. '1000E×8IP'.

Figure 3 shows that the stable flow stress and the corresponding $\tilde{M}(m)$ are sensitive to the mesh resolution and grain discretization. The 1000 element RVE with one integration point gives the highest Taylor factors, and correspondingly the highest extrapolated Taylor factor $M = 3.02$ in Table 1. When 8 integration points per element were used, for the RVE with one element per grain (1000E×8IP), the value of $\tilde{M}(m)$ significantly decreased. The flow stress and the value of $\tilde{M}(m)$ decreased when applying higher mesh resolution RVEs. The function $\tilde{M}(m)$ increases with decreasing $m$ for all RVEs.

Table 1 shows that the Taylor factor $M$ drops from 3.02 with the RVE with only one element and one integration point per grain to 2.68 with the finest mesh. The two finest meshes provide quite similar results, indicating that they both can be applied to define the new reference value of the Taylor factor as $M$= 2.7.

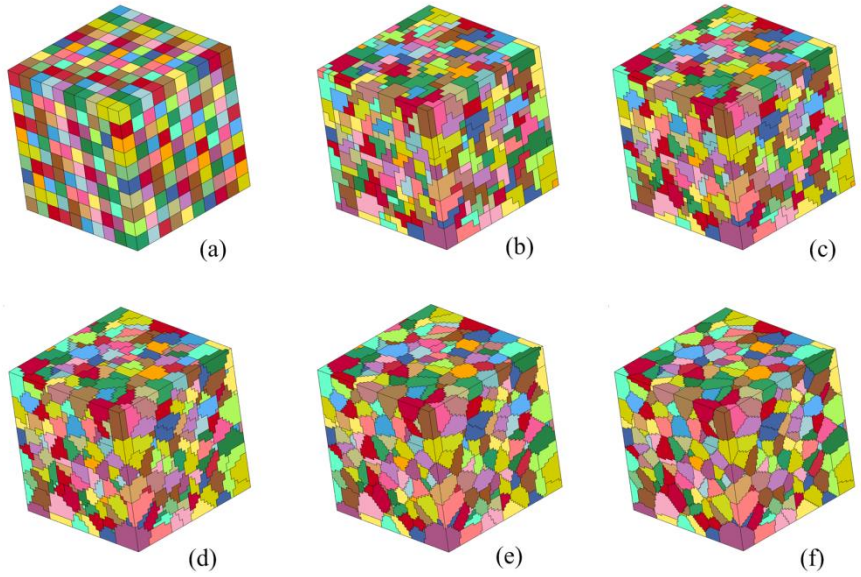


Figure 2. FEM meshes of the RVEs with (a) 1000 elements, (b) 8000 elements, (c) 27000 elements, (d) 64000 elements, (e) 216000 elements and (f) 512000 elements

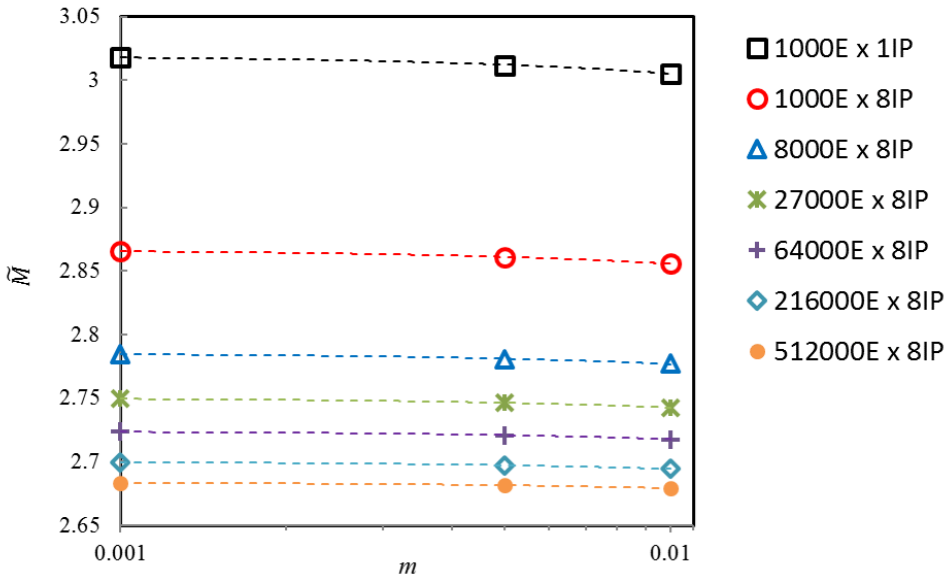


Figure 3. Data points and linear extrapolation functions for $\tilde{M}(m)$ simulated by CPFEM (E – element; IP - integration points per element).

Table 1 The calibrated values for the extrapolated Taylor factor $M$ from calculations by CPFEM with different numbers of elements and integration points.

| | 1000E×1IP | 1000E×8IP | 8000E×8IP | 27000E×8IP | 64000E×8IP | 216000E×8IP | 512000E×8IP |
|---|---|---|---|---|---|---|---|
| $M$ | 3.02 | 2.87 | 2.79 | 2.75 | 2.72 | 2.70 | 2.68 |

## 4.2 Isotropic yield-function exponent by CPFEM

The exponent $a$ of the yield function influence the curvature of the yield locus. Due to experimentally challenges in determining a precise estimation of the exponent $a$, it is seldom properly resolved by mechanical tests. Instead, stress states provided by CP calculations are used to calibrate this parameter of the yield function (Grytten et al., 2008; Saai et al., 2013; Zhang et al., 2014a; Zhang et al., 2015). The exponent $a$ of the isotropic yield function in Eq. (1) has been already calibrated by the FC-Taylor model and ALamel-type models (Zhang et al., 2015), which are rate-independent crystal plasticity models. In this section, the isotropic yield function exponent will be calibrated using CPFEM calculations. The influences of both the mesh resolution and the strain rate sensitivity $m$ on the calibration will be considered. Particularly, the exponent corresponding to the CPFEM with $m \to 0$ will be extrapolated.

Methods for generating stress points at yielding by CPFEM have been proposed in the literature (Saai et al., 2013), where periodic boundary conditions are applied. The principle idea is to varies the displacement velocities applied on the master nodes of the RVE and determine the corresponding flow stress. The flow stress in the CPFEM calculation is determined at a prescribed plastic work per unit volume. The volume averaged Cauchy stress tensor of all integration points is considered as the stress state at yielding. By systematically varying the prescribed velocities at different master nodes, a finite number of various stress states at yielding can be obtained and used for the calibration of the yield function. Details of this stress-point generating method are referred to the literature (Saai et al., 2013; Zhang et al., 2014a). It should be noted that even though the rate-independent yield surface does not really exist for rate dependent models (Van Houtte and Van Bael, 2004), the surface at yielding calibrated by the above method is the equi-plastic potential surface, which degenerates into a unique shape at the zero strain rate sensitivity limit. In this limit this equi-plastic potential surface acts as a yield surface with similar shape.

Since random orientations associated with isotropic material is considered here, the discretized $\sigma_{11}-\sigma_{22}$ yield locus section is calculated by CPFEM and assumed sufficient to calibrate the exponent $a$. Due to the increased computation time of CPFEM, only two RVEs with 1000 and 64000 elements (Figure 2. a and d), both with eight integration point per element, were employed in the CPFEM simulations to investigate the effect of the FE mesh resolution. To investigate the effect of the strain rate sensitivity $m$, the values of $m$=0.01 and $m$=0.005 were evaluated. A total of 119 strain paths were simulated for each RVE with each value of $m$. The strain-paths were distributed almost uniformly in the $\dot{\varepsilon}_{11}-\dot{\varepsilon}_{22}$ space. The stress states at the discretized yield loci were determined at the same plastic power per unit volume, 0.1 MPa, which corresponded to a true strain of about 0.4% in a uniaxial tensile test simulated by CPFEM. The yield surface exponent was then calibrated for each of these four series of 119 stress points at yielding. The calibration procedure is described in Zhang et al. (2014a). The calibration results are listed in Table 2, while the calibration quality can be assessed from Figure 4 , where a good agreement is found between the calibrated Hersey yield locus and the discrete stress points calculated with 64000 elements in the RVE and $m=0.01$.

Table 2 shows that the isotropic yield function exponent $a$ depend both on the mesh resolution and on $m$. The calibration based on the FE simulations with $1000\text{E} \times 8\text{IP}$ RVE is around 7.7, which is considerably smaller than the values calibrated using the classical rate-independent FC-Taylor model (Zhang et al., 2015). When increasing the mesh resolution to $64000\text{E} \times 8\text{IP}$, the exponent $a$ further decreased to below 7.0, which indicates a rounder yield surface. Applying RVEs with higher resolutions to generate the same number of stress-points will be extremely computational-time costly, and hence only five discrete stress points have been calculated using the finest RVE, i.e. with $512000\text{E} \times 8\text{IP}$, by CPFEM with $m = 0.01$. These five stress points are also included in Figure 4 *,* and almost perfectly match the calibrated yield locus from the 64000 element RVE. Hence, it is expected that the exponent $a$ will change little when the mesh resolution is $64000\text{E} \times 8\text{IP}$ or higher.

With smaller values of $m$ higher values of the exponent $a$ were obtained. However, the yield surface exponent *a* slightly changes when $m$ is decreased from 0.01 to 0.005. The dependence of the exponent *a* on the rate-sensitivity *m* for random orientations using a rate-dependent crystal plasticity has been reported in Mánik and Holmedal (2014), for the case of a Taylor-type iso-strain assumption. Examining the results there, a linear relationship between *a* and *m* can be observed for small values of *m*, i.e. when *m* is smaller than 0.1. Therefore, the exponent *a* for the rate-independent response, i.e. $m = 0$, can be linearly extrapolated from the results for $m = 0.01$ and for $m = 0.005$. The extrapolated values are included in Table 2. The value 6.9 is then obtained as the new reference values for the exponent of the Hershey yield function for FCC metals with random orientations, based on the CPFEM calculations.

Table 2 Calibrated and estimated values for the exponent of the isotropic yield function with different numbers of integration points and *m*. The value of *a* at *m=0* is linearly extrapolated.

| | $1000\text{E} \times 8\text{IP}$ | | | $64000\text{E} \times 8\text{IP}$ | | |
|---|---|---|---|---|---|---|
| *m* | 0.01 | 0.005 | 0 | 0.01 | 0.005 | 0 |
| *a* | 7.65 | 7.76 | 7.86 | 6.62 | 6.76 | 6.90 |

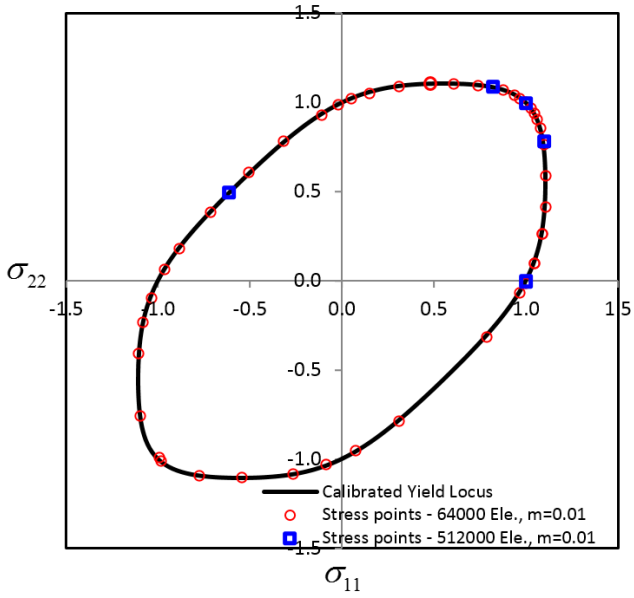


Figure 4 Yield locus calibrated using the stress states computed by CPFEM with the RVE of 64000 elements and $m = 0.01$. A limited number of stress states by CPFEM was plotted to enable a visual comparison. The stress states calculated by CPFEM with the RVE of 512000 and $m = 0.01$ are plotted on the top of the figure by square blue marker.

## 5 Quantitative analysis of crystal plasticity solutions

It is well known that relaxed constraint models give smaller Taylor factors, where the Sachs model (Sachs, 1928) provides the lower bound solution. Table 3 represents the value of Taylor factor *M* under uniaxial tensile test and the exponent *a* determined by different crystal plasticity models for FCC material with random orientations. The results by FC-Taylor and ALamel-type models are cited from a previous work (Zhang et al., 2015). The stress points for estimating the exponent *a* for the Sachs model were calculated as the average of the grains, when the stress was taken as the minimum required to activate any slip system. Note that the exponent from the Sachs model is very close to the Von Mises yield surface, which is obtained with *a*=2 or 4. The VPSC (Tomé and Lebensohn, 2009) results were extrapolated to $m \to 0$ using the methods presented in sections 3 and 4, and further detailed for VPSC computations in Appendix B.

Table 3 Taylor factor *M* for a uniaxial tensile test and estimated exponents *a* of the Hershey isotropic yield function, based on CP simulations for random orientations FCC metals. The VPSC results were extrapolated to *m*=0.

| CP models | *M* | *a* |
|---|---|---|
| FC-Taylor | 3.067 | 8.5 |
| ALamel | 2.826 | 6.6 |
| ALamel-T3 | 2.732 | 6.5 |
| VPSC | 2.80 | 6.9 |
| CPFEM | 2.684 | 6.9 |
| Sachs | 2.24 | 4.5 |

From the results in Table 1 compared to Table 2 and Table 3, it can be concluded that the advanced Taylor models with relaxed constraints and CPFEM with different mesh resolutions give smaller value of *M* than the FC-Taylor reference values. The VPSC and the ALamel-type models are based on quite different simplifications of the CPFEM model, but provide similar values of *M* and *a* as CPFEM with the finest mesh. It is of interest to look closer at their predictions. Hence, this chapter is attributed to quantitative analysis of the statistical deviations of $\mathbf{L}$, $\mathbf{D}^p$ and $\boldsymbol{\sigma}$ from the solutions by a reference model. In practice, the FC-Taylor solution has well defined corner solutions and equal velocity gradients in all grains and hence will serve as the reference solution for the comparisons.

## 5.1 Measures used for the analysis

When applying CPFEM or relaxed-constraint CP models, the local deformation at each considered integration point or grain may deviate from what is prescribed by the velocity gradient tensor $\mathbf{L}^{\mathrm{RVE}}$ of the global RVE. This local deviations of $\mathbf{L}$ and $\mathbf{D}^p$ can be quantified in similar way as the Schmitt angle for abrupt strain path changes (Schmitt et al., 1994). In this work, an angle $\theta_{D^p}$ is calculated from the normalized inner product between $\mathbf{D}^p$ at the local grain (or integration point) and $\mathbf{D}^{p,\mathrm{RVE}}$ at the RVE, as a measure of the deviation of $\mathbf{D}^p$ at each grain (or integration point) from the global deformation of the RVE, i.e.

$$\cos\left(\theta_{D^p}\right) = \frac{\mathbf{D}^p : \mathbf{D}^{p,\,\mathrm{RVE}}}{\left\|\mathbf{D}^p\right\| \cdot \left\|\mathbf{D}^{p,\,\mathrm{RVE}}\right\|}. \tag{16}$$

A corresponding angle $\theta_L$ is similarly defined for the deviation between the local velocity gradient at the grain (or integration point) $\mathbf{L}$ and at the RVE $\mathbf{L}^{\mathrm{RVE}}$.

$$\cos\left(\theta_L\right) = \frac{\mathbf{L} : \mathbf{L}^{\mathrm{RVE}}}{\left\|\mathbf{L}\right\| \cdot \left\|\mathbf{L}^{\mathrm{RVE}}\right\|} . \tag{17}$$

According to the Bishop-Hill analysis (Bishop, 1953; Bishop and Hill, 1951a, b), the particular stress tensor that accommodates an imposed strain mode, can be found by selecting from the 28 (56 with negatives) permissible FCC poly slip stress corners, the one that maximizes the external work. The CPFEM and the relaxed constraints CP models prescribe a mixed condition for the stress tensor and velocity gradient components; hence the local stress $\boldsymbol{\sigma}$ does not have to be a corner solution. The closest stress corner obtained by using the Bishop-Hill theory and imposing the local plastic velocity gradient $\mathbf{L}^p$, is employed as a reference corner stress tensor termed $\boldsymbol{\sigma}_{\mathrm{BH}}$. It is of interest to measure how far the local stress is from its closest corner solution. In this work, this is measured by the angle $\theta_\sigma$:

$$\cos\left(\theta_\sigma\right) = \frac{\boldsymbol{\sigma}'_{\mathrm{BH}} : \boldsymbol{\sigma}'}{\left\|\boldsymbol{\sigma}'_{\mathrm{BH}}\right\| \cdot \left\|\boldsymbol{\sigma}'\right\|} . \tag{18}$$

Another reference stress corner is the one corresponding to the RVE deformation as prescribed by $\mathbf{L}^{p,\mathrm{RVE}}$, i.e. defining the angle $\theta_\sigma^{\mathrm{RVE}}$ between the local stress $\boldsymbol{\sigma}$ and the FC-Taylor solution $\boldsymbol{\sigma}_{\mathrm{BH}}^{\mathrm{RVE}}$.

$$\cos\left(\theta_\sigma^{\mathrm{RVE}}\right) = \frac{\boldsymbol{\sigma}'^{\mathrm{RVE}}_{\mathrm{BH}} : \boldsymbol{\sigma}'}{\left\|\boldsymbol{\sigma}'^{\mathrm{RVE}}_{\mathrm{BH}}\right\| \cdot \left\|\boldsymbol{\sigma}'\right\|} . \tag{19}$$

All the randomly chosen grain orientations have each their corner solution $\boldsymbol{\sigma}_{\mathrm{BH}}^{\mathrm{RVE}}$.

## 5.2 Results for the polycrystalline under uniaxial tensile test

For the uniaxial tensile test, the prescribe velocity gradient tensor $\mathbf{L}^{\mathrm{RVE}}$ has components $L_{11}^{\mathrm{RVE}} = 2L_{22}^{\mathrm{RVE}} = 2L_{33}^{\mathrm{RVE}}$ with $L_{ij}^{\mathrm{RVE}} = 0$ for $i \neq j$. The uniaxial test simulations with CPFEM, as described in section 4.1 with $m$ = 0.01, were performed for the RVEs

illustrated in Figure 2. The angles $\theta_L$ , $\theta_{D^p}$ , $\theta_\sigma$ and $\theta_\sigma^{\mathrm{RVE}}$ were calculated for all integration points at an engineering strain of 0.5%. The uniaxial tensile test calculations with the ALamel-type model and the VPSC model (its numerical implementation by Tomé and Lebensohn (2009), *m* = 0.02 and *neff* = 10 intermediate linearization scheme, no grain co-rotation, no work hardening) were performed on a RVE with random orientations consisting of 5832 orientations. The angles $\theta_L$ , $\theta_{D^p}$ , $\theta_\sigma$ and $\theta_\sigma^{\mathrm{RVE}}$ were determined for each grain orientation.

Figure 5 illustrates the distribution of $\theta_L$ and $\theta_{D^p}$ obtained by the different RVEs and models described above using a bin step size of 2°. It is clearly shown that with increasing mesh resolution for the CPFEM, both $\theta_L$ and $\theta_{D^p}$ curves are shifted towards higher angles, i.e. deviating more from the RVE deformation as prescribed by the velocity gradient. The ALamel and ALamel-T3 models show broad peaks in Figure 5 , quite similar to the CPFEM results with the finest mesh. Interestingly, the VPSC has almost same distributions with respect to $\theta_L$ and $\theta_{D^p}$. The distributions of $\theta_L$ and $\theta_{D^p}$ reveal two major peaks for each; and the most dominant one occurs around 30°. Contrary to the VPSC model, CPFEM and the ALamel models show a distinct peak shift of about 10° between the $\theta_L$ and $\theta_{D^p}$ distributions.

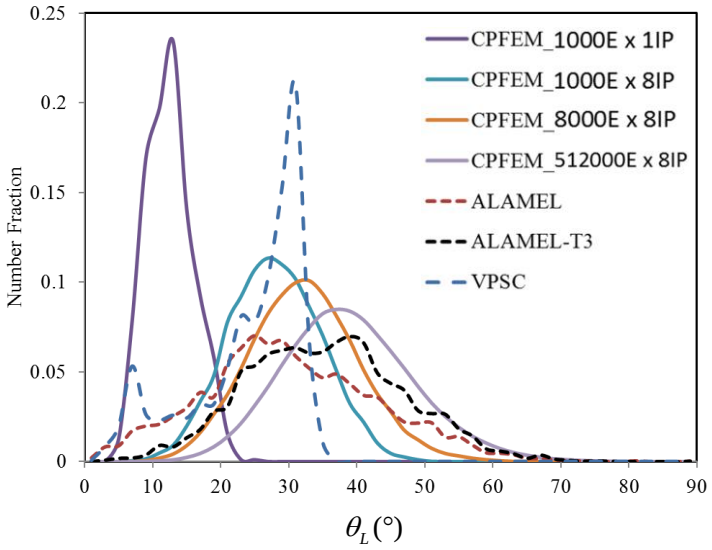


(a)

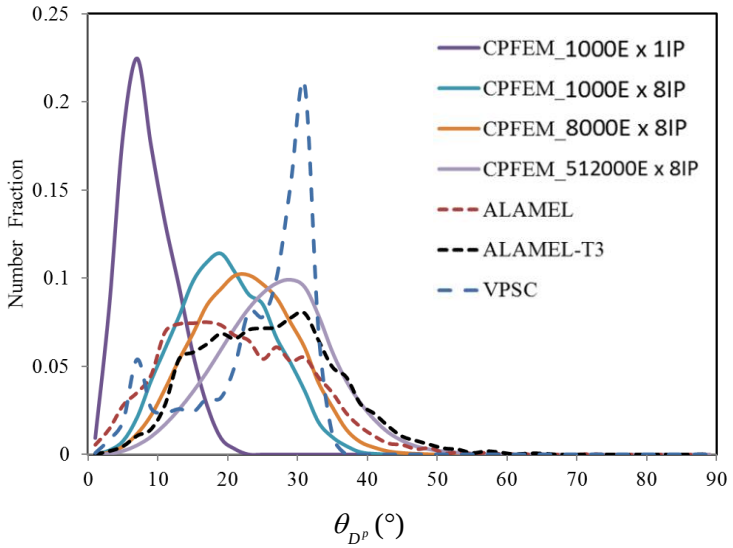


(b)

Figure 5 Distribution of $\theta_L$ (a) and $\theta_{D^p}$ (b) in terms of number fraction using a bin step size of 2° for the uniaxial tensile deformation. Solid lines are for CPFEM, for which the peaks move from left to right with increasing mesh resolution.

The distributions of $\theta_\sigma$ and $\theta_\sigma^{\mathrm{RVE}}$ are shown in Figure 6 (a) and (b), respectively. only the coarsest mesh ($1000\mathrm{E} \times 1\mathrm{IP}$), the fine mesh with $64000\mathrm{E} \times 8\mathrm{IP}$ and the finest mesh ($512000\mathrm{E} \times 8\mathrm{IP}$) are included in Figure 6. The distributions obtained by CPFEM are almost similar for all RVEs. In Figure 6 (a), the CPFEM solution has a significant peak at small values of $\theta_\sigma$, revealing that many local solutions are corner solutions, but with a broad weaker peak up to about 25º. The ALamel and ALamel-T3 models have very similar distributions that are qualitatively in agreement with the CPFEM distributions, but with a weaker corner peak and a stronger broad peak. The VPSC model is lacking the corner peak, but it has significantly stronger maximum intensities of the broad peak in the range 14° to 20°.

The distribution of $\theta_\sigma^{\mathrm{RVE}}$ is shown in Figure 6 (b), and illustrates the deviations of stress states from the FC-Taylor corner solution. In the case of CPFEM, the mesh size clearly affects the distribution of $\theta_\sigma^{\mathrm{RVE}}$. Compared to CPFEM solutions with the coarsest mesh, the number fraction for $\theta_\sigma^{\mathrm{RVE}} \leq 2^\circ$ is smaller for CPFEM with 512000E, and a broad spread is seen around 45º. Note that in the case of the most refined mesh, the CPFEM corner solution peak is considerably higher for the $\theta_\sigma$ distribution than for the $\theta_\sigma^{\mathrm{RVE}}$

distribution. Furthermore, it has a second peak around 45º, i.e. close to another neighbour corner solution compared to the FC-Taylor solution $\boldsymbol{\sigma}_{\mathrm{BH}}^{\mathrm{RVE}}$.

In the case of ALamel and ALamel-T3, the $\theta_{\sigma}^{\mathrm{RVE}}$ and $\theta_{\sigma}$ distributions in Figure 6 are qualitatively similar to those obtained with CPFEM, but contains fewer solutions at small angles close to the corner solutions and a stronger broad distribution up to 45º. The ALamel model is the only one amongst the considered Taylor type of models that has a $\theta_{\sigma}^{\mathrm{RVE}}$ peak at 45º, i.e. other corners than the FC-Taylor model. This is similar to the high resolution CPFEM distribution, but with lower magnitude. In the case of VPSC model, the distributions in Figure 6 are qualitatively different from the CPFEM solutions, since the corner solutions are almost absent for the VPSC model, and it has a peak at about 14º, both for $\theta_{\sigma}$ and for $\theta_{\sigma}^{\mathrm{RVE}}$.

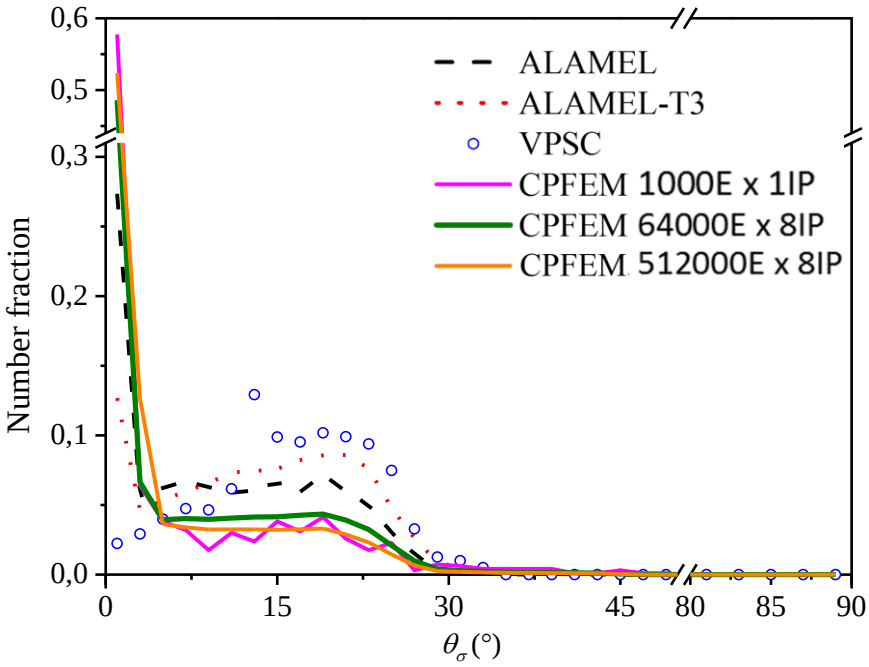


(a)

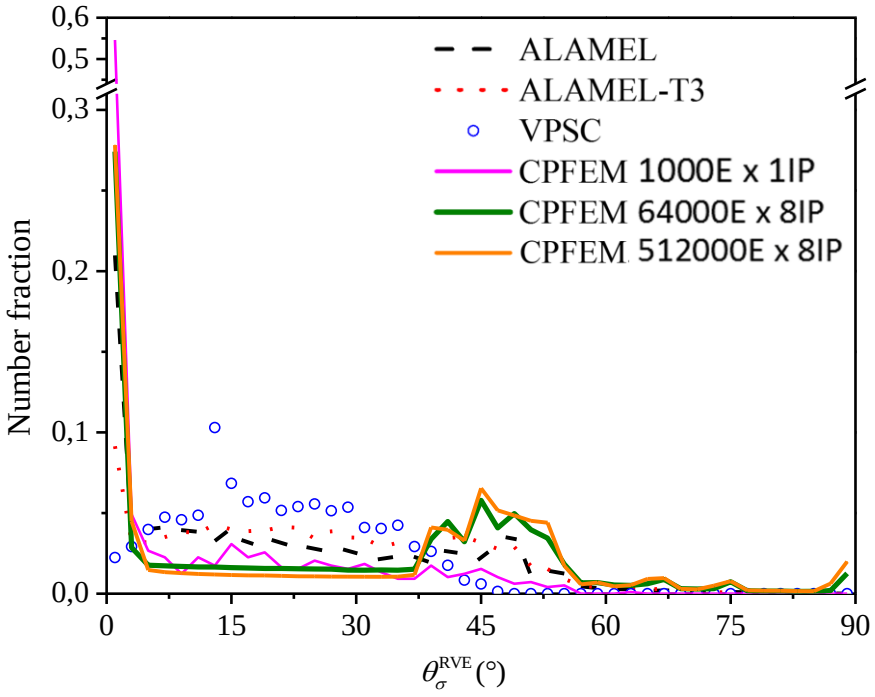


(b)

Figure 6 Distribution of (a) $\theta_\sigma$ and (b) $\theta_\sigma^{\mathrm{RVE}}$ in terms of number fraction using a bin step size of 2°.

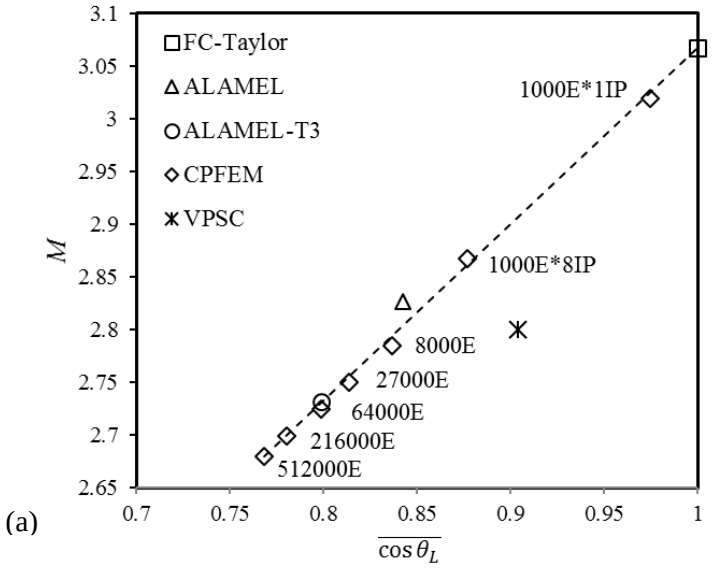
FC-Taylor
ALAMEL
ALAMEL-T3
CPFEM
VPSC
1000E*1IP
1000E*8IP
8000E
27000E
64000E
216000E
512000E
M
$\overline{\cos\theta_L}$

(a)

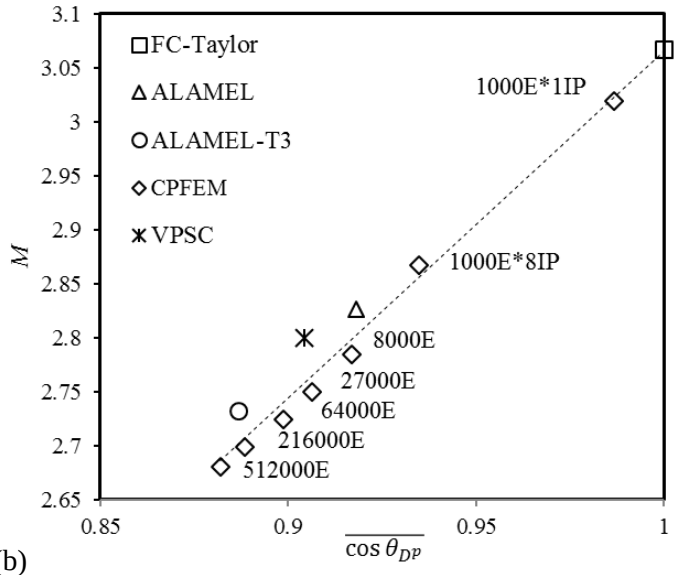
FC-Taylor
ALAMEL
ALAMEL-T3
CPFEM
VPSC
1000E*1IP
1000E*8IP
8000E
27000E
64000E
216000E
512000E
M
$\overline{\cos\theta_{Dp}}$

(b)

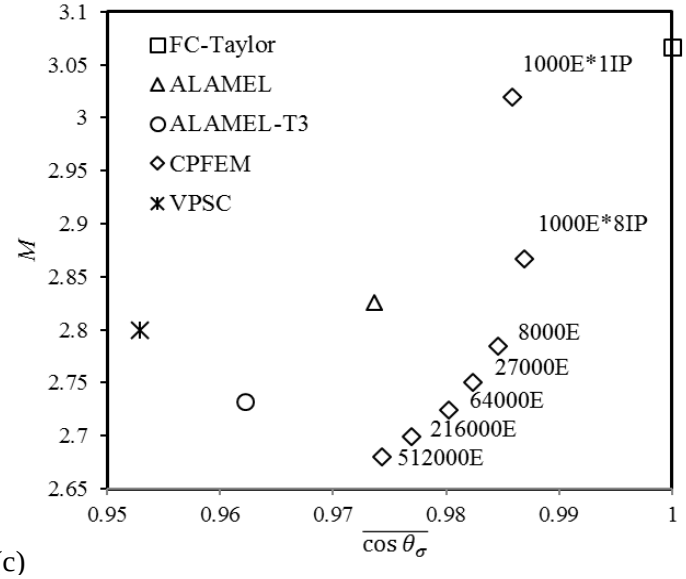
FC-Taylor
ALAMEL
ALAMEL-T3
CPFEM
VPSC
1000E*1IP
1000E*8IP
8000E
27000E
64000E
216000E
512000E
M
$\overline{\cos\theta_\sigma}$

(c)

Figure 7 The Taylor factor *M* versus the averages values of: (a) $\overline{\cos(\theta_L)}$ , (b) $\overline{\cos(\theta_{D^p})}$ and (c) $\overline{\cos(\theta_\sigma)}$ . The value of *m* = 0.01 is applied for CPFEM and *m* = 0.02 is applied for VPSC.

The Taylor factor *M* (extrapolated value to *m=0* in the case of CPFEM and VPSC) are plotted in Figure 7 (a), (b) and (c) versus the average values of $\overline{\cos(\theta_L)}$, $\overline{\cos(\theta_{D^p})}$ and $\overline{\cos(\theta_\sigma)}$, respectively, taken over all integration points and elements (grains). Except for the VPSC, all CP models in Figure 7 (a) fall on an approximately linear relationship between *M* and $\overline{\cos(\theta_L)}$. Figure 7 (b) shows that all models, including the VPSC model, falls on a linear relationship between *M* and $\overline{\cos(\theta_{D^p})}$. The relationship between *M* and $\overline{\cos(\theta_\sigma)}$ in Figure 7 (c) is more complex. With increasing mesh resolutions, the CPFEM solutions result in a decreased Taylor factor, but without decreasing $\overline{\cos(\theta_\sigma)}$ as much as the relaxed models, i.e. it contains many solutions closer to corner solutions. On the other hand, the VPSC model has the smallest $\overline{\cos(\theta_\sigma)}$.

## 5.3 Intra-granular variations under uniaxial tensile test

Unlike in the Taylor-type models, an orientation spread develops within each grain in CPFEM with a fine-meshed RVE. The spread of the stress and velocity gradient tensors within each grain, are analysed. The deviation angle between the average stress of the grain $\boldsymbol{\sigma}_g$ and the stress $\boldsymbol{\sigma}$ in a considered integration point, can be calculated as:

$$\cos\left(\theta_\sigma^g\right) = \frac{\boldsymbol{\sigma}'_g : \boldsymbol{\sigma}'}{\left\|\boldsymbol{\sigma}'_g\right\| \cdot \left\|\boldsymbol{\sigma}'\right\|} \ . \tag{20}$$

In a similar way, the deviation angle between the average velocity gradient of the grain $\mathbf{L}_g$ and the velocity gradient $\mathbf{L}$ of one of its integration points can be calculated as:

$$\cos\left(\theta_L^g\right) = \frac{\mathbf{L}_g : \mathbf{L}}{\left\|\mathbf{L}_g\right\| \cdot \left\|\mathbf{L}\right\|} . \tag{21}$$

The average angles $\overline{\theta_\sigma^g}$ and $\overline{\theta_L^g}$ calculated for all grains in the RVE and with m=0.01 are plotted in Figure 8. As expected, the intra-granular spreads of $\boldsymbol{\sigma}$ and $\mathbf{L}$ increase with increasing mesh resolution.

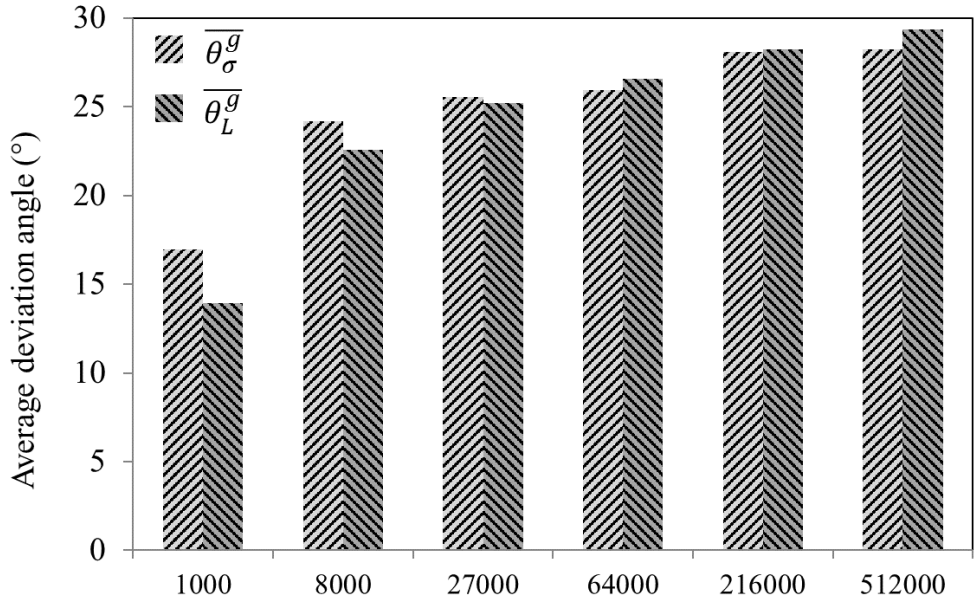


Figure 8 The averages $\overline{\theta_\sigma^g}$ and $\overline{\theta_L^g}$ of all average deviations in each grain $\theta_\sigma^g$ and $\theta_L^g$ for CPFEM simulations with different mesh resolutions, $m$=0.01.

## 6 Discussion and assessment of crystal plasticity models

Since the Taylor-type models are statistical aggregate models, only statistical features can be compared to the detailed CPFEM solutions. The ALamel, ALamel-T3 and VPSC models predict Taylor factors and yield surface exponents not too far from the CPFEM prediction with the finest mesh. Therefore, these two parameters are not sufficient to assess these aggregate models as simplified solutions of the CPFEM. More nuanced differences can be studied by quantifying statistically the amount of strain-constraint relaxations. In this work, strain deviations of the local $\mathbf{L}$ and $\mathbf{D}^p$ tensors with respect to the global ones are studied. Furthermore, stress deviations of the local stress tensors from their closest corner solution and from the FC-Taylor corner solution for the RVE are investigated.

In the case of rate-independent crystal plasticity models, a slip system is activated only when the resolved shear stress reaches the critical stress. The slip systems contribute to the yield surface by hyperplanes in the five-dimensional deviatoric stress space. These hyperplanes intersect and constitute the single crystal yield surface, which is a polyhedron in the five-dimensional space (Bishop and Hill, 1951a). Each facet of the five-dimensional polyhedron is bounded by corners and hyper-edges between them.

The yield locus of an FCC single crystal consists of 56 corners, which are of two kinds: 32 of them are intersections of 8 hyperplanes while 6 hyperplanes intersect in the remaining 24 corners, i.e. corner solutions may activate either up to 6 or up to 8 slip systems simultaneously. There are also solutions which could activate less than 5 slip systems, as shown in (Kocks, 1960), at lower-dimensional intersections or on facets of the single crystal yield surface, see also Mánik and Holmedal (2014). In the FC-Taylor model, almost all solutions are one of the 56 corner solutions. Since $\mathbf{D}^p$ is prescribed in this model, the chance is very small that its orientation is exactly normal to some of the aforementioned hyperplanes or hyperedges, i.e. a non-corner solution. On the contrary, relaxing the constraints of the velocity gradient tensor leads to imposing constraints on the stress. Under such conditions, the stress state will more seldom be identified in a corner. It follows that, in the FC-Taylor model, $\mathbf{L}$ and $\mathbf{D}^p$ are equal as for the RVE, and that $\theta_L$ and $\theta_{D^p}$ remain zero for all its grains. The shift of the peaks in the $\theta_L$ and $\theta_{D^p}$ distributions with increasing mesh resolutions of the RVE in CPFEM (see Figure 5 ) reflects a higher amount of local deviations from the RVE deformation mode. The curves for the ALamel and ALamel-T3 models roughly have the same shape as for the CPFEM, indicating that statistically they give similar amounts of strain relaxations.

Unlike the ALamel models, the VPSC model shows quite different distributions of $\theta_L$ and $\theta_{D^p}$ compared to the CPFEM, featuring double peaks. Furthermore, all CP models fall approximately onto a linear relationship between *M* and $\overline{\cos(\theta_{D^p})}$ in Figure 7 (b), whereas the VPSC model does not when *M* instead is plotted against $\overline{\cos(\theta_L)}$ in Figure 7 (a). This difference also reflects that statistically the VPSC contains a different distribution of the $\mathbf{W}$ tensors compared to the other models.

As demonstrated by Van Houtte et al. (2005) and Zhang et al. (2015), full strain compatibility and partial stress equilibrium can be fulfilled at common grain boundaries in ALamel-type models, while both strain compatibility and stress equilibrium can be fully fulfilled only in CPFEM, at least in a weak form sense. The similarity in the way ALamel-type models and CPFEM are dealing with local grain interactions may explain the similarity of their local deformation deviations, i.e. similar distributions of $\theta_L$ and

$\theta_{D^p}$. However, long range interactions between the two ALamel clusters and the rest of the grain aggregate are not accounted for. The VPSC model considers only long-range interactions between the grain and the surrounding homogeneous equivalent medium. The local inter- and intra- grain interactions are ignored in this type of model.

For the uniaxial tensile deformation mode, $\mathbf{L}=\mathbf{D}$, and the skew part of the velocity gradient $\mathbf{W}=0$. Hence, the shift as predicted by the high-resolution CPFEM towards smaller angles for the $\theta_{D^p}$ peak in Figure 5 (a) as compared to the $\theta_L$ peak in Figure 5 (b) is due to local variations of $\mathbf{W}$, which will influence the predictions of the texture evolution. It is interesting to note that the CPFEM, ALamel and ALamel-T3 models agree on a shift of about 10°, while the VPSC model hardly predict any shift. For the tensile deformation mode, it can be showed analytically that

$$\frac{\cos\left(\theta_L\right)}{\cos\left(\theta_{D^p}\right)}=\frac{\left\|\mathbf{D}^p\right\|}{\sqrt{\left\|\mathbf{D}^p\right\|^2+\left(\dot{\gamma}_1^{\mathrm{RLX}}\right)^2/2+\left(\dot{\gamma}_2^{\mathrm{RLX}}\right)^2/2+\left(\dot{\gamma}_3^{\mathrm{RLX}}\right)^2/2}}\leq 1 \qquad (22)$$

where $\dot{\gamma}_r^{\mathrm{RLX}}$ ($r$=1, 2, 3) is the relaxation shear rates defined in the ALamel (Van Houtte et al., 2005) and ALamel-T3 models (Mánik and Holmedal, 2013). This means that the shift in the ALamel models is caused by the grain interaction of the two grains in the considered cluster. It is reasonable to assume that the shift in CPFEM is also mainly due to the local interactions between neighbouring grains. Such interactions are modelled by the ALamel and ALamel-T3, while the VPSC model considers long interactions with the average of the grains contained by the RVE, and hence fails to predict this shift.

Some of the VPSC deviations from CPFEM could also been due to the fact that the 1-site inclusion formalism used in VPSC solves independently the equilibrium equation for each inclusion embedded in the effective medium. This does not account for spatial stress gradients inside grains and across grain boundaries and leads to errors in fulfilling the virtual work principle (Turner et al., 1999). Additional simulations using the second order update (Liu and Castaneda, 2004) were performed. These calculations are more time consuming and less numerically stable with decreased strain rate sensitivity. They showed very similar results related to the distributions of $\theta_{D^p}$ and $\theta_L$ as with the 1-site inclusion formalism; hence these solutions were not included in Figure 5.

Local corner solutions, say for $\theta_\sigma < 2^\circ$ (see Figure 6), are observed for all investigated models. These are solutions that locally maximize the plastic work. The CPFEM model contains many corner solutions, both with coarse and fine mesh. About 50% of the stress solutions are corner solutions. In the case of the coarse mesh, almost all of the corners are the FC-Taylor corners for the corresponding RVE. This holds for only about half of the local corners with the fine mesh, where the corresponding peak around 45° in Figure 6 (b) denotes neighbor corner solutions as compared to the FC-Taylor corner solutions for the corresponding RVE. Note, that the three smallest angles between two Bishop-Hill stress corners are 40.9°, 45° or 52.2°.

The ALamel and ALamel-T3 models have a qualitatively similar distribution of $\theta_\sigma$ as the CPFEM in Figure 6 (a). However, only about 25% of ALamel solutions and 10% of ALamel-T3 solutions are local corner solutions, and most of these corners are equal to the FC-Taylor corners for the corresponding RVE. The relaxation of the strain constraints in these models creates too many non-corner solutions as compared to CPFEM, in particularly the ALamel-T3.

The VPSC has almost none corner solutions. A distribution with greater fractions of corner solutions could be obtained by changing the interaction parameter *neff*, so that the model becomes closer to the FC-Taylor model. However, the texture predictions, the Taylor factor and the yield surface exponent in this case would become more similar to the FC-Taylor model and little would be gained as compared to CPFEM.

The corners in the 5-dimensional stress space are very sharp. Hence, corner solutions will result in considerable higher stress components. The decaying Taylor factor with increased strain rate sensitivity for the FC-Taylor model (Mánik and Holmedal, 2014) occurs because the yield surface corners becomes more rounded. Similarly, the ALamel-type and VPSC models give smaller Taylor factors (Table 3) due to their accounts of interactions, either locally or long-range type, respectively. This enables a high amount of non-corner solutions, which gives smaller stress components. The Taylor factor by the ALamel-T3 is slightly smaller than the one by the ALamel model, because of the additional relaxation assumed in ALamel-T3. All the above-mentioned results are consistent with the commonly accepted qualitative understanding of the influence of relaxation on Tylor Factor. Taylor factor is smaller than the upper bound

FC-Taylor solution when the strain-constraints are relaxed. The stronger the relaxation, the smaller is the Taylor factor (Delannay, 2001).

The high resolution CPFEM solution, however, still contains a high number of corner solutions. Still, the corresponding Taylor factor is equally small as for the advanced Taylor models. The good resolution of the RVE in the CPFEM provides better abilities to resolve the inter- and intra- grain interactions (Zhao et al., 2007; Zhao et al., 2008), to maintain the local stress equilibrium and thereby to relax the strain-constraints as compared to the Taylor model. Many of the solutions will still be corner solutions, but about half of these belong to different corners than the FC-Taylor model. This disperses the solutions so that the RVE homogenization of the stress results in smaller stress components and contributes to a smaller Taylor factor as shown in Table 1. The relationship between $M$ and $\overline{\cos(\theta_\sigma)}$ in Figure 7 (c) illustrates that in the case of Taylor-type models, the Taylor factor decreases with increased amount of strain relaxations. In the case of CPFEM, Taylor factor decreases with refined mesh resolution at higher values of $\overline{\cos(\theta_\sigma)}$, due to large amount of corner solutions. A key issue to further improve the advanced Taylor models is to allow the type of local interactions that can give a higher number of non-FC-Taylor corner solutions. The ALamel model can do this to some extent, as seen from the 45° peak in Figure 6.

Figure 8 demonstrates that the average in-grain spread of deformation and stress increases with the grain discretization in the CPFEM's RVE. With the increasing RVE resolution, the number of integration points positioned at grain boundaries decreases as compared to the total number of integration points in the grain. Interestingly, the decrease of the Taylor factor and of the yield surface exponent associated to CPFEM highlight that the intra-grain interactions are as much important as the local interactions at the grain boundaries. The local grain pair interactions were accounted for in the ALamel-type models and can be interpreted both in terms of grain boundary interactions and more general influence of a neighbour grain. Accounting for these local interactions provides statistical distributions of stress and strain rate tensors that are much closer to CPFEM than the VPSC model, which considers long-range interactions between the grain and the surrounding homogeneous equivalent medium.

# 7 Conclusions

CPFEM calculations with refined grains resolution were performed to provide precise estimation of the Taylor factor and the yield surface exponent for the reference case of random orientations, in the limit of rate-independent plasticity. It is concluded that the new reference values of Taylor factor and yield surface exponent equal respectively 2.7 and 6.9. This is in agreement with recent estimates by state-of-the-art relaxed-constraints variants of the Taylor model.

The local deformation at each grain in CPFEM or relaxed-constraint CP models deviate from what is prescribed by the velocity gradient tensor of the global RVE. These local deviations were quantified in this work using $\theta_L$ and $\theta_{D^p}$. The stress deviations of the local stress tensors from their closest corner solution and from the FC-Taylor corner solution were also studied. The statistical distributions of these parameters were used to assess ALamel-type models and VPSC model compared to CPFEM solutions. The ALamel models predicts similar statistical distributions of stress corner deviations as the CPFEM, whereas the VPSC model predicts far too few corner solutions. For the specific case of a tensile test, a characteristic peak shift between the $\theta_L$ and $\theta_{D^p}$ distributions is analytically explained based on the grain interactions by the ALamel-type models and also predicted by the CPFEM simulations. The VPSC model does not account for short range interactions and hence fails to predict this shift. Even though the ALamel models and the VPSC model all predict almost the same yield surface exponent and Taylor factor as the CPFEM, the VPSC model does not match the statistical distributions from the CPFEM simulations. The consideration of short range grain interactions in the ALamel model seems to be more important than accounting for long-range interactions and the surrounding homogeneous equivalent medium assumption in the VPSC model. The intra-grain analysis for CPFEM demonstrates that the intra-grain interactions are as much important as the local interactions at the grain boundaries.

## Appendix A Derivation of the Taylor factor $\tilde{M}$ for strain rate sensitive metals

The rate-dependent formulation described in Section 2 will be made dimensionless for the case of a uniaxial tensile deformation along the 1-direction and random orientations. It is assumed constant $D_{11}$ component of the strain rate tensor **D** and constant value of initial (reference) resolved shear stress for all slip systems $\tau_0^\alpha = \tau_0$. Dimensionless variables are obtained by scaling, and are represented by a tilde above the original symbol.

The dimensionless time $\tilde{t}$ is defined as

$$\tilde{t} = t \cdot D_{11} \tag{23}$$

Hence, the kinematic variables can be scaled by the reciprocal of $D_{11}$, for example

$$\begin{aligned} \tilde{\dot{\gamma}}^\alpha &= \dot{\gamma}^\alpha / D_{11} \\ \tilde{\mathbf{D}} &= \mathbf{D} / D_{11} \\ \tilde{\mathbf{W}} &= \mathbf{W} / D_{11} \end{aligned} \tag{24}$$

The dimensionless stress $\tilde{\boldsymbol{\sigma}}$ is defined as

$$\tilde{\boldsymbol{\sigma}} = \boldsymbol{\sigma} \cdot \left[ \frac{1}{\tau_0} \left( \frac{\dot{\gamma}_0}{D_{11}} \right)^m \right] . \tag{25}$$

Hence, the dimensionless revolved shear stress $\tilde{\tau}^\alpha$ turns to be

$$\tilde{\tau}^\alpha = \tau^\alpha \cdot \left[ \frac{1}{\tau_0} \left( \frac{\dot{\gamma}_0}{D_{11}} \right)^m \right] = \tilde{\boldsymbol{\sigma}} : \mathbf{P}^\alpha \ . \tag{26}$$

By combining Eqs. (11) and (26), one gets

$$\tilde{\dot{\gamma}}^\alpha = \dot{\gamma}^\alpha / D_{11} = \left| \tilde{\tau}^\alpha \right|^{\frac{1}{m}} \operatorname{sgn}(\tilde{\tau}^\alpha) \ . \tag{27}$$

As seen from Eq. (25) the dimensionless stress component $\tilde{\sigma}_{11}$ becomes equal to the Taylor factor *M* in the limit when *m* goes to zero. Hence for any strain rate sensitivity *m*, it can be regarded as the rate-dependent Taylor factor, $\tilde{M} = \tilde{\sigma}_{11}$, listed in Eq. (14)

## Appendix B Extrapolations of VPSC results to its rate-independent limit

The Taylor factor was calculated using the uniaxial tensile test performed by the VPSC code by Tomé and Lebensohn (2009). A total of 1241 strain rate directions which were nearly evenly distributed, were applied to generate the corresponding stress points at yielding. These stress points were then applied to calibrate the Hershey isotropic yield function exponent.

A selection of 5832 random orientations were input into the VPSC. The intermediate linearization scheme with *neff* = 10 was applied, see Tomé (1999). No grain co-rotation or work hardening were considered here. The uniaxial tensile test was performed with four different values of *m* in the VPSC model, which were 0.02, 0.05, 1/12 and 0.1, respectively, while only the first three values were applied when calibrating the yield surface exponent. Eq. (15) was adopted to fit Taylor factor for the VPSC results for the uniaxial tensile tests, and a linear extrapolation was performed for the exponent. The results are presented in Figure. B- 1 where both the calculated results and the fitted curves are shown. In the rate-independent limit with the VPSC model, the Taylor factor *M* and the exponent *a* were then 2.80 and 6.91, respectively.

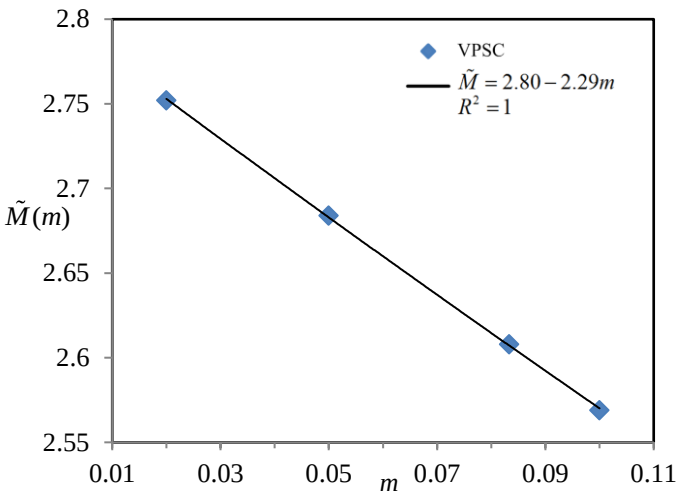


(a)

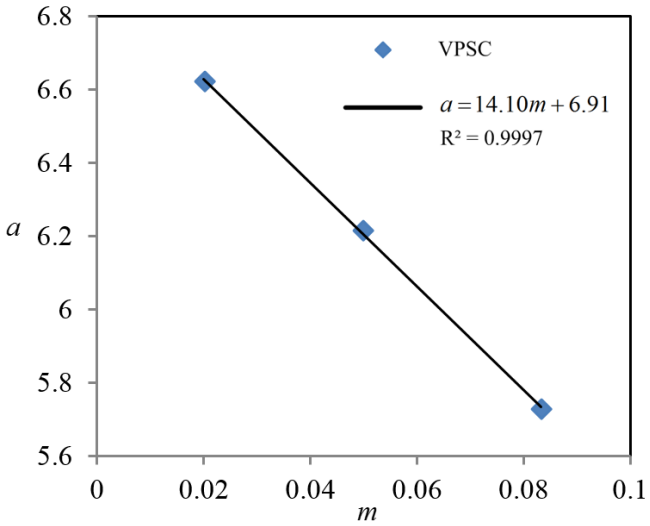


(b)

Figure. B- 1 a) Extrapolation of the Taylor factor *M*, and b) of the Hershey isotropic yield function exponent *a* to the rate-independent limits of *m=0* for the VSPC calculations.

# References


Aretz, H., Barlat, F., 2013. New convex yield functions for orthotropic metal plasticity. Int. J. Nonlin. Mech. 51, 97-111.

Banabic, D., 2010. Plastic Behaviour of Sheet Metal, Sheet Metal Forming Processes. Springer Berlin Heidelberg, pp. 27-140.

Banabic, D., Aretz, H., Comsa, D.S., Paraianu, L., 2005. An improved analytical description of orthotropy in metallic sheets. Int. J. Plast. 21, 493-512.

Barlat, F., 1987. Crystallographic texture, anisotropic yield surfaces and forming limits of sheet metals. Mater. Sci. Eng. 91, 55-72.

Barlat, F., Aretz, H., Yoon, J.W., Karabin, M.E., Brem, J.C., Dick, R.E., 2005. Linear transfomation-based anisotropic yield functions. Int. J. Plast. 21, 1009-1039.

Barlat, F., Richmond, O., 1987. Prediction of tricomponent plane stress yield surfaces and associated flow and failure behavior of strongly textured f.c.c. polycrystalline sheets. Mater. Sci. Eng. 95, 15-29.

Bishop, J.F.W., 1953. A Theoretical Examination of the Plastic Deformation of Crystals by Glide. Philos. Mag. 44, 51-64.

Bishop, J.F.W., Hill, R., 1951a. A Theoretical Derivation of the Plastic Properties of a Polycrystalline Face-Centred Metal. Philos. Mag. 42, 1298-1307.

Bishop, J.F.W., Hill, R., 1951b. A Theory of the Plastic Distortion of a Polycrystalline Aggregate under Combined Stresses. Philos. Mag. 42, 414-427.

Blum, W., Zeng, X.H., 2009. A simple dislocation model of deformation resistance of ultrafine-grained materials explaining Hall–Petch strengthening and enhanced strain rate sensitivity. Acta Mater. 57, 1966-1974.

Bunge, H.J., 1970. Some applications of the Taylor theory of polycrystal plasticity. Kristall und Technik 5, 145-175.

Canova, G.R., Wenk, H.R., Molinari, A., 1992. Deformation Modeling of Multiphase Polycrystals - Case of a Quartz Mica Aggregate. Acta Metall. Mater. 40, 1519-1530.

Delannay, L., 2001. Observation and modelling of grain interactions and grain subdivision in rolled cubic polycrystals Departement Metaalkunde en Toegepaste Materiaalkunde. KU Leuven.

Dunand, M., Maertens, A.P., Luo, M., Mohr, D., 2012. Experiments and modeling of anisotropic aluminum extrusions under multi-axial loading – Part I: Plasticity. International Journal of Plasticity 36, 34-49.

Grytten, F., Holmedal, B., Hopperstad, O.S., Børvik, T., 2008. Evaluation of identification methods for YLD2004-18p. Int. J. Plast. 24, 2248-2277.

Han, J.-H., Kim, D.-I., Jee, K.-K., Oh, K.H., 2004. Evolution of crystallographic orientations in an aluminum single crystal during tensile deformation. Mater. Sci. Eng., A 387–389, 60-63.

Hershey, A., 1954. The plasticity of an isotropic aggregate of anisotropic face centred cubic crystals. Journal of Applied Mechanics 21, 241-249.

Holmedal, B., 2015. Strength contributions from precipitates. Philos. Mag. Lett. 95, 594-601.

Hosford, W.F., 1972. A Generalized Isotropic Yield Criterion. Journal of Applied Mechanics 39, 607-609.

Hughes, D.A., Hansen, N., 2018. The microstructural origin of work hardening stages. Acta Materialia 148, 374-383.

Iadicola, M.A., Foecke, T., Banovic, S.W., 2008. Experimental observations of evolving yield loci in biaxially strained AA5754-O. International Journal of Plasticity 24, 2084-2101.

Kanjarla, A.K., Van Houtte, P., Delannay, L., 2010. Assessment of plastic heterogeneity in grain interaction models using crystal plasticity finite element method. Int. J. Plast. 26, 1220-1233.

Kocks, U.F., 1958. Polyslip in Polycrystals. Acta Metall. 6, 85-94.

Kocks, U.F., 1960. Polyslip in single crystals. Acta Metall. 8, 345-352.

Kocks, U.F., 1970. The relation between polycrystal deformation and single-crystal deformation. Metall and Materi Trans 1, 1121-1143.
Kocks, U.F., Mecking, H., 2003. Physics and phenomenology of strain hardening: the FCC case. Prog. Mater Sci. 48, 171-273.
Kuwabara, T., 2007. Advances in experiments on metal sheets and tubes in support of constitutive modeling and forming simulations. International Journal of Plasticity 23, 385-419.
Kuwabara, T., Umemura, M., Yoshida, K., Kuroda, M., Hirano, S., Kikuta, Y., 2006. Forming limit strains of 5000 series aluminum alloys with different magnesium contents. Journal of Japan Institute of Light Metals 56, 323-328.
Kuwabara, T., Yoshida, K., Narihara, K., Takahashi, S., 2005. Anisotropic plastic deformation of extruded aluminum alloy tube under axial forces and internal pressure. International Journal of Plasticity 21, 101-117.
Lebensohn, R.A., Tomé, C.N., 1993. A self-consistent anisotropic approach for the simulation of plastic deformation and texture development of polycrystals: Application to zirconium alloys. Acta Metall. Mater. 41, 2611-2624.
Lebensohn, R.A., Tomé, C.N., 1994. A self-consistent viscoplastic model: prediction of rolling textures of anisotropic polycrystals. Mater. Sci. Eng., A 175, 71-82.
Lequeu, P., Gilormini, P., Montheillet, F., Bacroix, B., Jonas, J.J., 1987. Yield Surfaces for Textured Polycrystals .1. Crystallographic Approach. Acta Metall. 35, 439-451.
Leyson, G.P.M., Curtin, W.A., Hector, L.G., Woodward, C.F., 2010. Quantitative prediction of solute strengthening in aluminium alloys. Nat Mater 9, 750-755.
Liu, Y., Castaneda, P.P., 2004. Second-order theory for the effective behavior and field fluctuations in viscoplastic polycrystals. J Mech Phys Solids 52, 467-495.
Mánik, T., Holmedal, B., 2013. Additional relaxations in the Alamel texture model. Mater. Sci. Eng., A 580, 349-354.
Mánik, T., Holmedal, B., 2014. Review of the Taylor ambiguity and the relationship between rate-independent and rate-dependent full-constraints Taylor models. Int. J. Plast. 55, 152-181.
Mecking, H., Kocks, U.F., Hartig, C., 1996. Taylor factors in materials with many deformation modes. Scripta Mater. 35, 465-471.
Molinari, A., Canova, G.R., Ahzi, S., 1987. A self consistent approach of the large deformation polycrystal viscoplasticity. Acta Metall. 35, 2983-2994.
Peirce, D., Asaro, R.J., Needleman, A., 1982. An analysis of nonuniform and localized deformation in ductile single crystals. Acta Metall. 30, 1087-1119.
Peirce, D., Asaro, R.J., Needleman, A., 1983. Material rate dependence and localized deformation in crystalline solids. Acta Metall. 31, 1951-1976.
Quey, R., Dawson, P.R., Barbe, F., 2011. Large-scale 3D random polycrystals for the finite element method: Generation, meshing and remeshing. Comput. Method, Appl. M. 200, 1729-1745.
Roters, F., Eisenlohr, P., Hantcherli, L., Tjahjanto, D.D., Bieler, T.R., Raabe, D., 2010. Overview of constitutive laws, kinematics, homogenization and multiscale methods in crystal plasticity finite-element modeling: Theory, experiments, applications. Acta Mater. 58, 1152-1211.
Saai, A., Dumoulin, S., Hopperstad, O.S., Lademo, O.G., 2013. Simulation of yield surfaces for aluminium sheets with rolling and recrystallization textures. Comput. Mater. Sci. 67, 424-433.
Sachs, G., 1928. Zur ableitung einer filebedingung. Zeitschrift des Vereines Deutscher Ingenieure 72, 734-736.
Schmid, E., Boas, W., 1935. Kristallplastizität: Mit besonderer Berücksichtigung der Metalle. Springer, Berlin.
Schmitt, J.H., Shen, E.L., Raphanel, J.L., 1994. A parameter for measuring the magnitude of a change of strain path: Validation and comparison with experiments on low carbon steel. Int. J. Plast. 10, 535-551.

Shiratori, E., Ikegami, K., 1968. Experimental study of the subsequent yield surface by using cross-shaped specimens. J Mech Phys Solids 16, 373-394.
Tadano, Y., Kuroda, M., Noguchi, H., 2012. Quantitative re-examination of Taylor model for FCC polycrystals. Comput. Mater. Sci. 51, 290-302.
Taylor, G.I., 1938. Plastic strain in metals. J. Inst. Metals. 62, 307-324.
Taylor, G.I., 1956. Strains in Crystalline Aggregate, in: Grammel, R. (Ed.), Internationale Union für Theoretische und Angewandte Mechanik / International Union of Theoretical and Applied Mechanics: Verformung und Fliessen des Festkörpers / Deformation and flow of Solids. Springer Berlin Heidelberg, Berlin, Heidelberg, pp. 3-12.
Taylor, G.I., Dehlinger, U., 1956. Strains in Crystalline Aggregate, in: Grammel, R. (Ed.), Deformation and Flow of Solids / Verformung und Fliessen des Festkörpers: Colloquium Madrid September 26–30, 1955 / Kolloquium Madrid 26. bis 30. September 1955. Springer Berlin Heidelberg, Berlin, Heidelberg, pp. 3-12.
Tomé, C.N., 1999. Self-consistent polycrystal models: a directional compliance criterion to describe grain interactions. Modell. Simul. Mater. Sci. Eng. 7, 723.
Tomé, C.N., Lebensohn, R.A., 2009. Manual for code Visco-Plastic Self-Consistent (VPSC).
Turner, P.A., Tome, C.N., Christodoulou, N., Woo, C.H., 1999. A self-consistent model for polycrystals undergoing simultaneous irradiation and thermal creep. Philos. Mag. A 79, 2505-2524.
Van Houtte, P., Li, S., Seefeldt, M., Delannay, L., 2005. Deformation texture prediction: from the Taylor model to the advanced Lamel model. Int. J. Plast. 21, 589-624.
Van Houtte, P., Van Bael, A., 2004. Convex plastic potentials of fourth and sixth rank for anisotropic materials. Int. J. Plast. 20, 1505-1524.
Vilamosa, V., Clausen, A.H., Børvik, T., Holmedal, B., Hopperstad, O.S., 2016. A physically-based constitutive model applied to AA6082 aluminium alloy at large strains, high strain rates and elevated temperatures. Materials & Design 103, 391-405.
Wu, P.D., MacEwen, S.R., Lloyd, D.J., Neale, K.W., 2004. Effect of cube texture on sheet metal formability. Materials Science and Engineering: A 364, 182-187.
Yoshida, K., Kuroda, M., 2012. Comparison of bifurcation and imperfection analyses of localized necking in rate-independent polycrystalline sheets. Int. J. Solids. Struct. 49, 2073-2084.
Zecevic, M., Knezevic, M., 2018. Latent hardening within the elasto-plastic self-consistent polycrystal homogenization to enable the prediction of anisotropy of AA6022-T4 sheets. International Journal of Plasticity.
Zhang, K., Holmedal, B., Hopperstad, O.S., Dumoulin, S., 2014a. Modelling the plastic anisotropy of aluminum alloy 3103 sheets by polycrystal plasticity. Modell. Simul. Mater. Sci. Eng. 22, 075015.
Zhang, K., Holmedal, B., Hopperstad, O.S., Dumoulin, S., Gawad, J., Van Bael, A., Van Houtte, P., 2015. Multi-level modelling of mechanical anisotropy of commercial pure aluminium plate: Crystal plasticity models, advanced yield functions and parameter identification. Int. J. Plast. 66, 3-30.
Zhang, K., Hopperstad, O.S., Holmedal, B., Dumoulin, S., 2014b. A robust and efficient substepping scheme for the explicit numerical integration of a rate-dependent crystal plasticity model. Int. J. Numer. Meth. ENG. 99, 239-262.
Zhao, Q., Holmedal, B., 2013. Modelling work hardening of aluminium alloys containing dispersoids. Philos. Mag. 93, 3142-3153.
Zhao, Z., Kuchnicki, S., Radovitzky, R., Cuitiño, A., 2007. Influence of in-grain mesh resolution on the prediction of deformation textures in fcc polycrystals by crystal plasticity FEM. Acta Mater. 55, 2361-2373.

Zhao, Z., Ramesh, M., Raabe, D., Cuitiño, A.M., Radovitzky, R., 2008. Investigation of three-dimensional aspects of grain-scale plastic surface deformation of an aluminum oligocrystal. Int. J. Plast. 24, 2278-2297.